A Model of a Combined ESA and ExB Probe

IEPC-2025-711

Presented at the 39th International Electric Propulsion Conference, Imperial College London, London, United Kingdom, 14-19 September 2025

Hendrix Price¹, Seth Thompson², Casey C. Farnell³, Cody C. Farnell⁴, and John D. Williams⁵ *Colorado State University, Fort Collins, CO, 80523, U.S.A.*

The Energy and Velocity Analyzer for Distributions of Electric Rockets (E-VADER) is a combined electrostatic analyzer (ESA) and ExB velocity filter designed to resolve species- and charge-statespecific ion energy distribution functions (IEDFs) in ion engine plumes. In this work, we present the first computational model of the E-VADER, coupling finite element field solutions with particletracking algorithms to evaluate diagnostic performance and quantify systematic and random errors in reconstructed IEDFs. Simulation campaigns explore error propagation across transmission energies and charge states, demonstrating the dependence of energy resolution, skew, and abundance fraction fidelity on probe operating conditions. Results show that while the E-VADER can generally reproduce species-specific distributions, systematic broadening and skew reduction occur at higher transmission energies, motivating error-correction approaches for experimental data. These findings are particularly relevant as the electric propulsion community investigates alternative propellants—including molecular species such as water, nitrogen, various chemical rocket propellants, and even air mixtures—for which traditional plume species characterization is very challenging. Moreover, as higher-power Hall thrusters are developed, neutral density effects inside probe bodies become increasingly relevant; a preliminary model for CEX-induced signal attenuation is thus presented and mitigation is discussed. By establishing the accuracy limits and operational sensitivities of the E-VADER, this study provides a foundation for its application to both conventional xenon and krypton Hall thrusters as well as nextgeneration propulsion concepts employing unconventional propellants.

¹ Graduate Research Assistant, Department of Mechanical Engineering, Hendrix.Price@colostate.edu.

² Research Scientist, Department of Mechanical Engineering, and Research Engineer at Plasma Controls, LLC, seth.thompson@colostate.edu.

³ Research Scientist, Department of Mechanical Engineering, and President Plasma Controls, LLC, casey.farnell@colostate.edu.

⁴ Research Scientist, Department of Mechanical Engineering, and President Plasma Controls, LLC, cody,farnell@colostate.edu.

⁵ Professor, Department of Mechanical Engineering, and Technical Director at Plasma Controls, LLC, john.d.williams@colostate.edu.

I. Introduction

The Energy and Velocity Analyzer for Distributions of Electric Rockets (E-VADER) is a combined electrostatic analyzer (ESA) and velocity filter (ExB) plasma diagnostic probe developed for characterization of plasma discharges. An axial-cross section top-view of the probe solid model is displayed in Fig. 1. The ESA sector serves to construct the ion energy distribution function (IEDF) of an ion plume through controlled deflection of ions down a spherical arc axis with a central angle of 120° and radius of 5 cm; this component and its neighbors are isolated in Fig. 2. Ions are selected over a complete input energy per charge range via a sweeping bias applied to the entrance collimator that accelerates them to an operator-designated "transmission energy" per charge while suppressing electron ingestion; this sweeping "scan" voltage V_s accelerates ions according to the relation

$$\varepsilon_f = \varepsilon_i + V_s \tag{1}$$

where ε denotes energy per charge, and i and f subscripts denote initial and final, respectively.^{4,5} This posits that the entering charged particles are accelerated precisely by the scan potential applied to the collimator at a particular setpoint on the sweep.

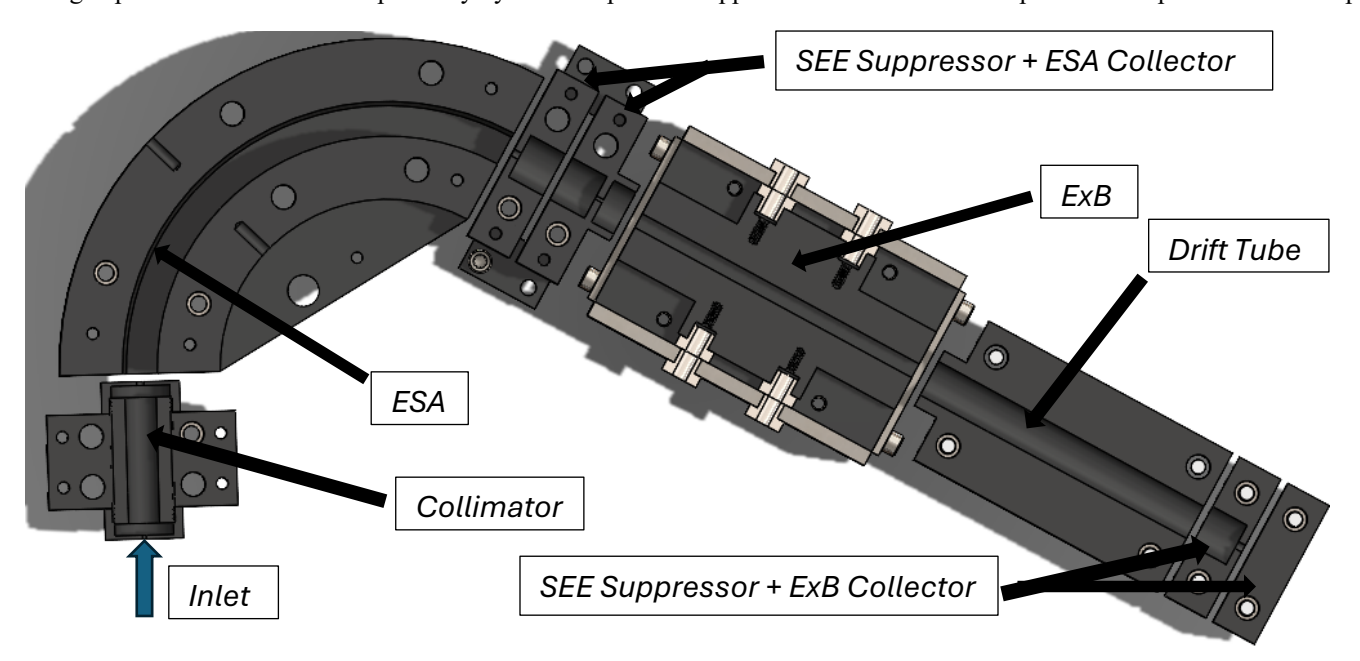


Figure 1. E-VADER solid model, axial cross section view.

When the final energy per charge of a slice of the IEDF is within the probe's bandpass of the set transmission energy per charge for a particular initial energy per charge, those ions transmit through the spherical ESA track, and the corresponding current is measured on a collection conductor. The current contributions at each applied scan voltage step are thus proportional to the probability density of the corresponding initial energy per charge in the ion plume, and the IEDF can be constructed via a comprehensive voltage sweep. This design allows the spherical plate potential difference, ΔV , to be maintained constant for an IEDF trace, which prevents propensity for variable bandpass error over a single energy trace; all ions that are transmitted and collected have the same transmission energy per charge. The spherical plate bias necessary to pass ions at the set transmission energy can be solved analytically to be

$$\Delta V = 2\varepsilon_T \ln \left(\frac{r_2}{r_1}\right) \approx \varepsilon_T \left(\frac{r_2}{r_1} - \frac{r_1}{r_2}\right) \qquad , \tag{2}$$



Figure 2. ESA + entrance collimator, suppressor, collector.

where ε_T is the transmission energy per charge and r_1 and r_2 are the inner and outer radii of the plates, respectively.

The ExB sector, displayed in Fig. 3, is arranged in-line with the ESA and functions to separate the transmitted ions according to their energies, i.e. masses and velocities, and by proxy, charge states. The latter is achieved because the ESA filters ions according to their energy per charge, so ions entering the ExB sector travel with energy multiples $E = E_i, 2E_i, 3E_i$, etc. corresponding with their charge states z = 1, 2, 3, etc.; ions are decelerated back to their initial energies per charge upon

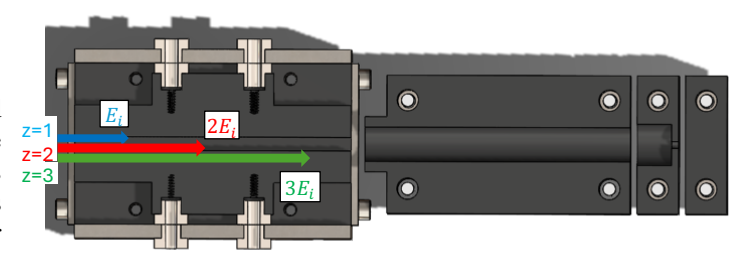


Figure 3. ExB + drift tube, suppressor, collector.

transmitting the ESA. The ExB probe leverages perpendicular, countervailing electric and magnetic fields to deflect ingested ions via the Lorentz force

$$\vec{F} = q(\vec{E} + \vec{v} \times \vec{B}) \tag{3}$$

which for idealized perpendicular fields prescribes the undeflected ion condition to be

$$|\vec{v}| = \frac{|\vec{E}|}{|\vec{B}|} = \frac{\Delta V}{Bd} \qquad , \tag{4}$$

where ΔV is the voltage difference between the biased, parallel plates and d is their separation distance. The applied potential to the plates at which the ions transmitted from the ESA sector will also transmit the ExB sector is thus governed by

$$\Delta V = Bd \sqrt{\frac{2q\varepsilon_i}{m}} \propto \sqrt{Z} \qquad , \tag{5}$$

where *B* is magnetic field strength, *q* is particle charge, *m* is particle mass, and *z* is charge state – this proportionality is emphasized specifically for atomic plasma plumes. This asserts that sweeping the biased plates for a selected ESA scan voltage generates completely deconvolved charge state peaks for the associated energy per charge location on the IEDF, allowing for a much cleaner resolution of the charge state distribution compared with a traditional, standalone ExB probe which ingests the entirety of the ion plume energy distribution at once. Species-specific IEDFs can be reconstructed from the ExB collector measurements by stepping through select ESA scan voltages to capture the charge state distributions for a series of discrete energy slices along the IEDF. The reconstructed species-specific IEDFs can be integrated to determine the relative abundance fractions of each species, as well as provide one-dimensional insights into the ionization physics of the thruster plume by intimating the electrostatic potentials where species are born.

The purpose of this study is to provide computational validation and source physical reasons for phenomena observed in the E-VADER's experimental datasets with the objective of quantifying random and correcting systematic uncertainties, predicting behavior under specific operating conditions, providing heuristics for the highest fidelity experimental procedure, and identifying engineering enhancements to improve future probe iterations. These objectives represent study end-goals and have not yet been systematically achieved nor are comprehensively discussed in this paper. This report does *not* present a thorough computational model; it does not simulate particle trajectories under the influence of all real excitations applied to the probe's sub-components, space-charge build-up, or electron effects. Its purpose is to present the first iteration of the model and provide rudimentary findings in constructing input distributions considering primary effects.

II. Methods

A. Finite Element Analysis

The model framework consists of field solutions from the computational FEA solver Ansys Maxwell as well as ion tracking infrastructure developed in Python. Ansys simulations were conducted on the comprising ESA and ExB solid models, including on their adjacent components to capture fringe field effects from the neighboring biased surfaces; the intrigue in the field simulations lies mostly in capturing these boundary effects that may influence ion trajectories in an unpredictable fashion. The solid model computational field solutions have been validated with analytical comparison as well as with physical measurement in the case of the ExB's magnetic field. The electric field behavior between the two ESA plates is solved from the Laplace equation in cylindrical coordinates

$$r^2 \frac{\partial^2 V}{\partial r^2} + r \frac{\partial V}{\partial r} + \frac{\partial^2 V}{\partial \theta^2} = 0 (6)$$

to be

$$\vec{E}(r) = \frac{-1}{\ln\left(\frac{r_2}{r_1}\right)} \frac{\Delta V}{r} \hat{r} \tag{7}$$

The electrostatic force, described with $\vec{F}(r) = q\vec{E}(r)$, can be equated with the definition of centripetal force to define the electric field in terms of the requisite tangential energy – the transmission energy – necessary for an ion to maintain a constant radius. This reduces Eq. (7) to

$$\vec{E}(r) = \frac{-2\varepsilon_T}{r}\hat{r} \qquad , \tag{8}$$

which is used to construct the analytical electric field solution in the model for use in validating the Ansys FEA solution. The analytical field solution between the biased parallel plates of the ExB sector is simply the standard "infinite parallel plates" solution

$$\vec{E}(z) = \frac{\Delta V}{d}\hat{z} \qquad , \tag{9}$$

where *d* is the separation of the plates. The magnetic field FEA was validated with physical linear measurement of the probe's on-axis field using a gaussmeter. The Ansys magnetic field solution overpredicts the magnitude of the flux density; this is likely due to inconsistency between the Sm-Co grade selection in the solid model and the magnets used in the physical probe. Simply scaling down the simulated magnitudes by the ratio of the experiment-to-FEA means of the on-axis fields calibrates the computational solution to good agreement with experiment. Shown below in Figs. 4 and 5 are on-axis comparisons between the FEA and corresponding validating analytical E-field solutions for both probe sectors as well as the experimental validation of the B-field. Validation can be demonstrated for off-axis components as well. The on-axis edge and fringe field behaviors are of principal interest in these presentations.

The 3d Ansys field solutions are imported into the Python framework and interpolated onto a mesh of user-defined resolution. Both probesectors in the E-VADER contain components of variable applied voltage, especially in the ExB where voltage steps are often refined to 0.1 V over sweeps from 0 V to 50 V. To circumvent the necessity of running FEA for all possible applied potentials, the electrostatic solution tensors between the biased plates of each sector are computed once at high voltage to minimize numerical noise and then divided by this voltage to obtain normalized electric field in units of 1/m. These tensor elements are then re-scaled to the appropriate electric field strength for a given voltage. This technique proves effective in quickly

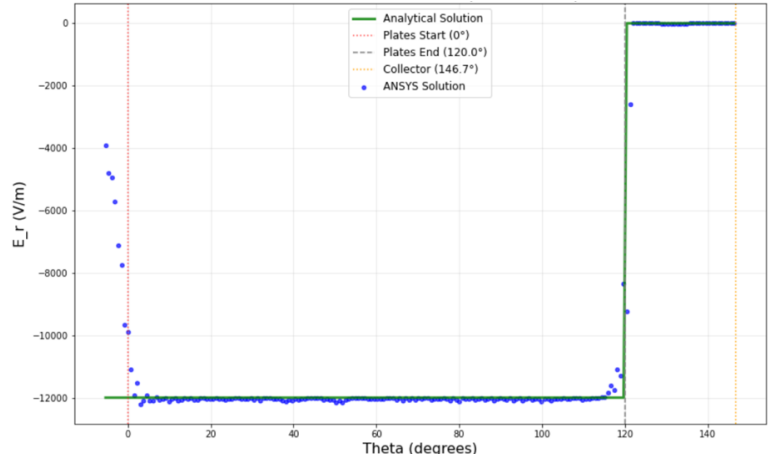


Figure 4. ESA sector FEA validation with analytical E-field solution from Eq. (8). The transmission energy, ε_T , is set to 300 eV/z.

and progressively updating electric field magnitudes while preserving valuable direction information, and it is used throughout the analysis presented in this paper.

B. Particle Generation & Acceleration

Ion stepping is conducted using a 4th order Runge-Kutta integrator in the ESA sector. Each simulated ion is accelerated through the probe by the field propagating from its nearest-neighbor mesh node in time-step intervals set by the user. Input IEDF moment parameters – location, scale, and shape – are selected by the user to define a skew-normal distribution for each input charge state to be simulated, overall charge state abundance fractions are selected, and each input distribution is area-normalized to its respective abundance fraction such that the area under the total (all charge states) IEDF is unity. Moreover, particle mass and total particles to simulate per ESA scan step, N_{pop} , are user-decided, and the distributions input constructed

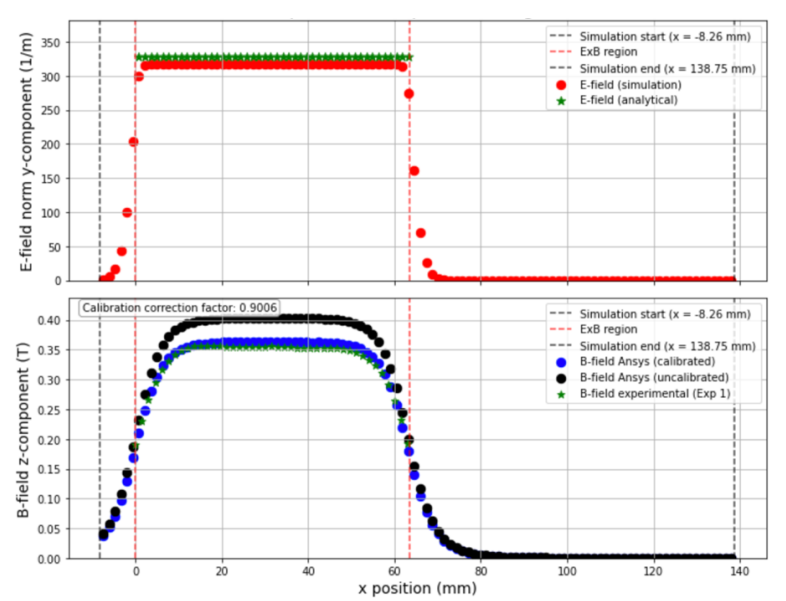


Figure 5. ExB sector FEA validation with analytical E-field solution and experimental B-field measurement.

deterministically using an inverse cumulative distribution function (CDF). The transmission energy per charge and initial energy per charge domain are also chosen, and the ions are pre-accelerated into the ESA by the sweeping collimator scan voltage matched with each step in the initial energy per charge domain necessary to accelerate the associated ions to the transmission energy. This is simply performed mathematically per Eq. (1) in this model iteration, without ion tracking through the collimator. The ions are injected single-file at the entrance of the ESA sector with start positions randomly sampled on a uniform distribution of diameter equivalent to the collimator exit. The start velocities are unidirectional in the tangential direction. N_{pop} ions, distributed over the charge state-specific input IEDFs according to their respective abundance fractions, are passed through the ESA at every scan voltage, and their termination positions are determined either to be on a probe wall or the ESA collector or its exit aperture, which allows ions to pass to the ExB sector for analysis. This final state data is stored, and those ions that are transmitted through the exit aperture can be exported into the ExB simulator.

The ExB particle mover leverages the Boris algorithm, a leapfrogging integrator commonly used for Lorentz force acceleration due to its second-order accuracy and ability to conserve particle energy. It performs alternating half-step electrostatic accelerations with magnetic rotations. Ions transmitted through the ESA's exit aperture at select scan voltages are accelerated through this sector at swept voltage biases with initial states corresponding with their final states stored by the ESA tracking. ExB termination states are determined, and those ions that reach the ExB collector are saved for species distribution analysis.

For the ESA simulation, the normalized collection results can be plotted with two techniques: (1) using the sampled input IEDFs to construct a collection count histogram with each *empirical* initial energy per charge to indicate the simulation's success in transmitting the energies according to their population densities in the input distribution, or (2) using each *theoretical* initial energy per charge given by its relationship with scan voltage and nominal transmission energy to construct the collection vs initial energy per charge distribution as a scatter plot. The latter technique is how the real probe software constructs the IEDFs because, naturally, no prior knowledge of the input distributions exists. The difference between the two techniques can highlight artificial shifting in the ESA-constructed IEDFs caused by systematic error induced by electric field uncertainties that shift the nominal transmission energy. This effect should not be present using the analytical electric field solution unless the ion-stepping integration method is implemented incorrectly, and thus the analytical solution is employed for preliminary validation of the particle acceleration infrastructure in Python.

Ion stepping for z=1, 2, 3 charge states at a transmission energy of 100 eV/z is exemplified below in Figs. 6a-c to demonstrate the requisite initial energies for each charge state for successful transmission to the back of the ESA sector. The ions with energies per charges within the bandwidth of the transmission energy per charge follow a near perfect arc between

the spherical plates and pass through the drift region, indicating successful ion stepping implementation with the Runge-Kutta integrator.

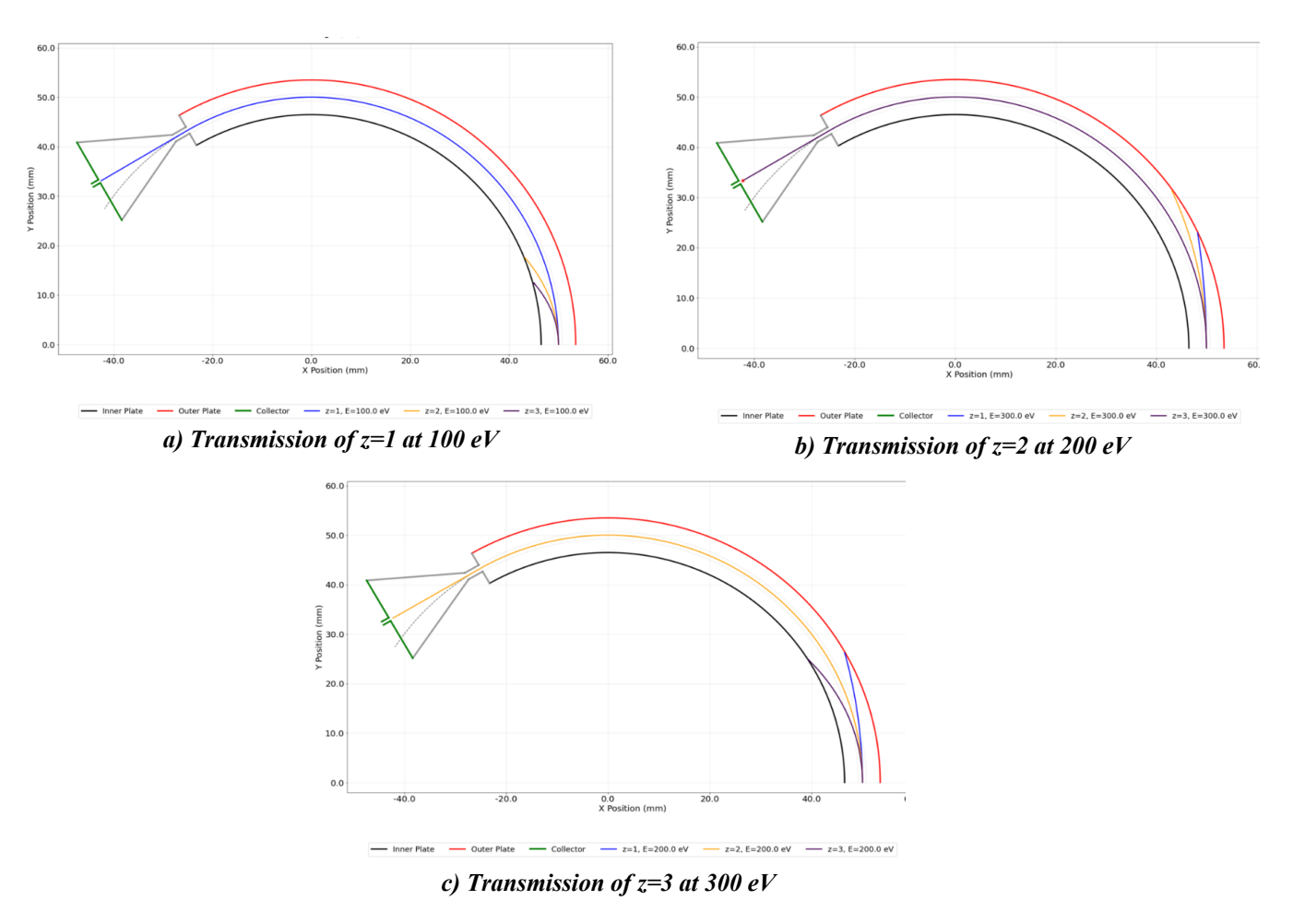


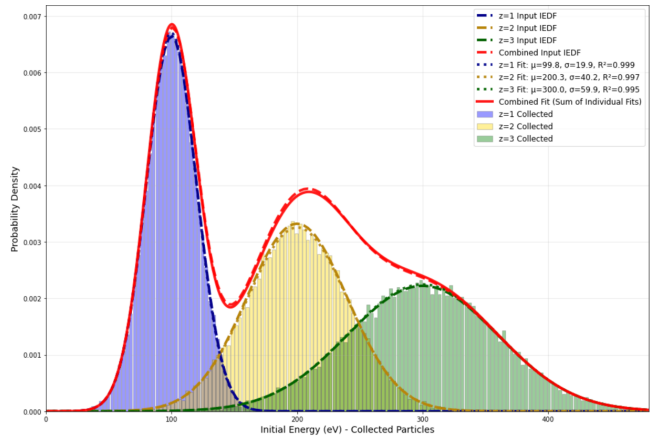
Figure 6a,b,c. Verification of transmission of a) z=1, b) z=2, c) z=3 ions at $\varepsilon_{trans}=100$ eV/z.

C. Validating ESA Simulation

A complete ESA simulation using the analytical electrostatic field solution is performed to fully validate the input ion energy distribution construction and time-stepping integrator. The simulation is executed with the input parameters displayed in Table 1, and the resulting histogram showing collection efficiency against 3.0 eV bins of empirical initial ion energy is depicted in Fig. 7. Figure 8 shows a collection scatter plot of the same simulated results using the theoretical transmission energy to solve for initial energies, the second technique discussed previously. Initial energy is the independent variable plotted instead of initial energy per charge, the traditional mode of IEDF construction, to separate the charge state IEDFs for visualization.

Table 1. Input IEDF parameters for ESA simulation.

	$\varepsilon_T = 300 \text{ eV/z}, m = 30 \text{ AMU}$		
	z=1	z=2	z=3
Mean (eV)	100	200	300
Standard Deviation	20	40	60
Rel. Abund.	0.333	0.333	0.334



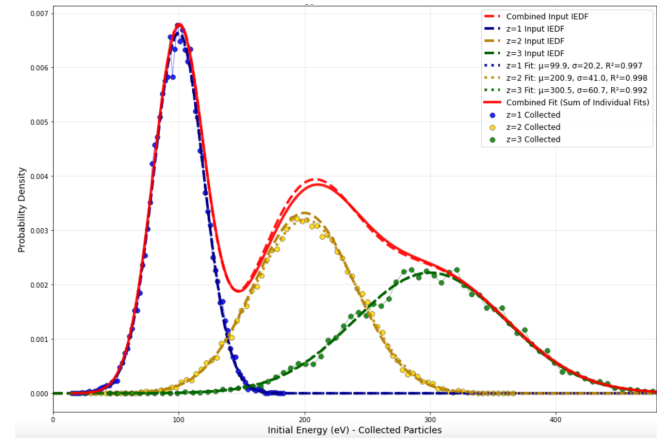


Figure 7. Normalized ESA collection results plotted against empirical initial energies.

Figure 8. Normalized ESA collection results plotted against expected initial energies.

Table 2 compares the collected abundance fractions with the input population, and good agreement is shown. Slight error is very likely the product of a mildly coarse mesh grid and the consequence of nearest neighbor acceleration, and this is observed in other simulations. It is evident that the base computational infrastructure of the simulation, i.e., particle generation, analytical field solving, and particle-stepping, has been implemented correctly because the empirical distribution of binned initial energies reconstructs the inputs precisely, and likewise does the discrete distribution plotted against theoretical initial energies derived from the selected transmission energy; these verifications are apparent from the close overlap between the input IEDFs and collection fit curves.

Table 2. Input abundance fractions compared with collected fractions.

	z=1	z=2	z=3
Input Rel. Abund.	0.333	0.333	0.334
Collected	0.335	0.328	0.337
% Error	0.60	1.5	0.90

D. Validating ExB Simulation

Sample particle-tracking for the transmission of the three charge states at arbitrary energies through the ExB sector under the influence of arbitrary applied electrostatic potentials is shown in Fig. 9a-c. The effect of the inequitable edge-field sag for the E- and B-fields demonstrated in Fig. 5 is evidenced by the curvature of the ion paths at the edges of the field regions. Time-stepping validation is performed by directly verifying energy conservation using the analytical E-field solution from Eq. (8) and a set, constant B-field. This calculation for example ions transmitted to the collector from a particular input parameter set is conducted and presented in Table 3. The near-perfect energy conservation for the three charge states demonstrates the accuracy of the Boris algorithm. In a similar fashion to the ESA codebase, a complete validation simulation was performed on the ExB codebase to confirm successful reproduction of input abundance fractions; this is not presented.

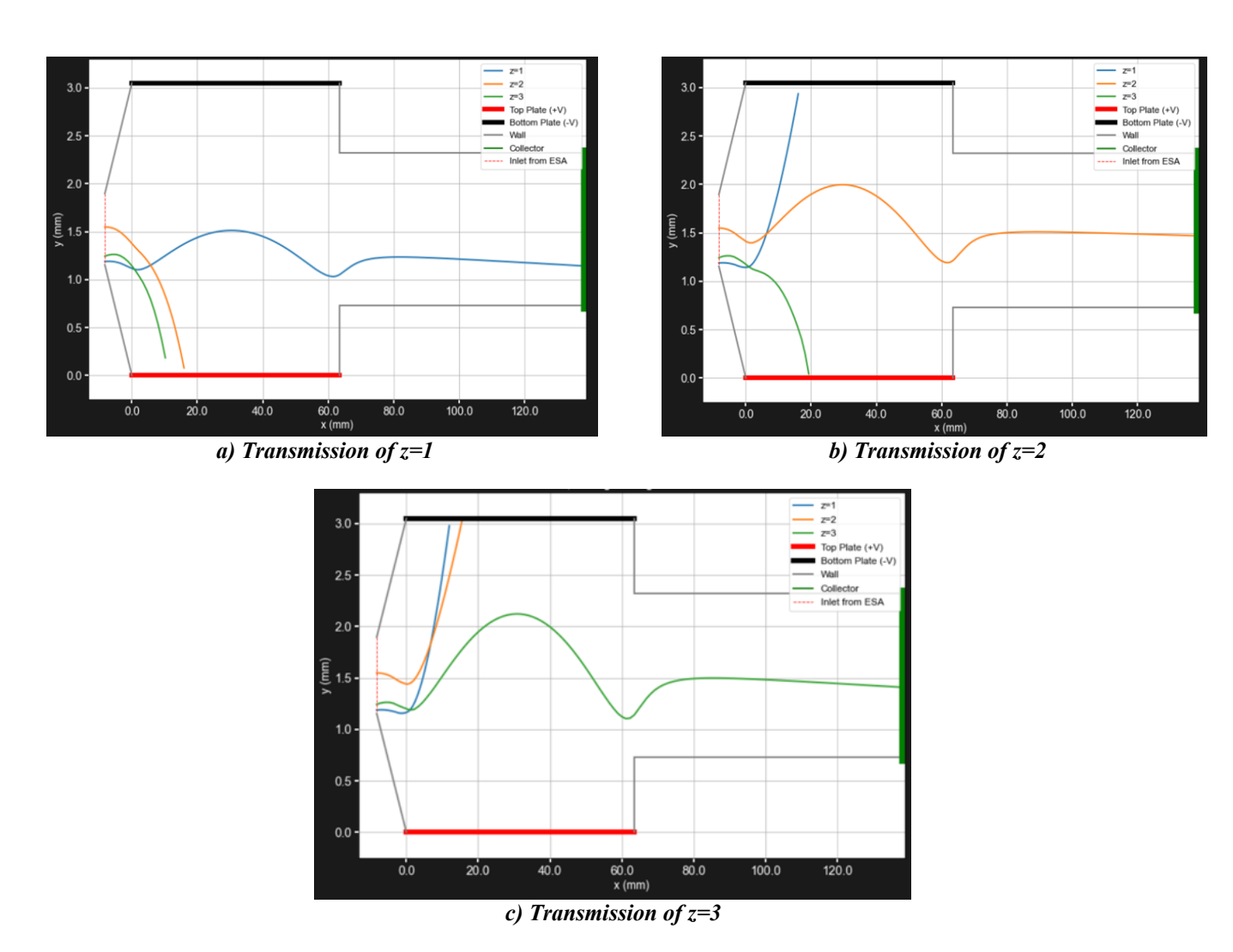


Figure 9a,b,c. Sample transmission of a) z=1, b) z=2, and c) z=3 ions through the ExB sector at nominal energies and ΔV values.

Table 3. Energy conservation of analytical ExB simulation.

	z=1	z=2	z=3
E_i (eV)	275.18	530.17	772.31
E_f	275.17	530.12	772.42
% Error	0.00	0.01	0.01

III. Results and Discussion

With satisfactory model verifications complete, particle-accelerating simulations employing the FEA field solutions on sophisticated input ion population parameter sets are executed to identify potential sources of systematic error within the E-VADER. Presented in this report is the analysis of a set of skew-normal charge-state IEDFs with disparate statistical moments; these inputs are explored across transmission energies to garner insight into how the accuracy of species-specific and total IEDF reconstruction performed by the ESA is transmission energy-dependent. Table 4 provides the statistical parameters for these simulation runs; note for skew-normal distributions, location and scale are used to define distributions. These are closely coupled to mean and standard deviation, respectively, and identical when no skew is present.

Table 4. Input parameters for skew-normal IEDFs.

	$\varepsilon_T = 475, 675, 875 \text{ eV/z}, m = 30 \text{ AMU}$		
	z=1	z=2	z=3
Location (eV/z)	300	280	276.67
Scale	8	25	8.33
Skew	2	6	-2
Rel. Abund.	0.70	0.25	0.05

A. ESA Simulation of Input Parameters

As briefly mentioned, despite the input populations being deterministic and completely repeatable, these ions are randomly and uniformly injected over the ESA's entrance orifice; this is the only source of statistical noise present in the input. Because of this, simulations at each condition need to be executed more than once to quantify the noise and parse it from systematic error. A much finer field mesh is instantiated for this simulation campaign to avoid approximation errors caused by the nearest-neighbor acceleration; however, this necessitates particle population per scan, N_{pop} , to be lower for reasonable runtimes. This, in turn, increases sensitivity to statistical noise. For the direct comparison of the figure of interest in this study, ε_T , the figures below simply display single examples of each transmission energy run, although noise is considered in quantitative analyses. Species-specific IEDF constructions via ESA simulation are shown for each of the three tested transmission energies in Figs. 10-12. Note these collection distributions are presented in the typical form of energy per charge, as the probe would construct the IEDF. The distribution statistics for each simulation are given in Table 5 for quantitative comparison. It is visually evident and verifiable from the statistical analysis that increasing transmission energy increases error in the width of each distribution. For the lowest transmission energy tested, 475 eV/z, overprediction of $\Delta E/E$ for each charge state is upwards of 50% for z=1 and 3; interestingly, the error for z=2 is significantly less, though still considerable. Input skew is very likely contributing to how well the IEDFs are constructed, but nonetheless there is no obvious trend in $\Delta E/E$ as it relates to charge state other than overall IEDF construction precision depreciating with transmission energy for all charge states. Because the transmission energy per charge must be set higher than the highest ion energy per charge passed through the ESA to suppress electrons, the bandpass error is unavoidable. Future work will be to characterize this error to high precision to allow for systematic correction of data measured at a particular transmission, and a probe re-design effort might be initiated to eliminate transmission of electrons into the ESA stage when ion energies higher than the transmission energy exist. Error in skew scales as well; each charge distribution approaches symmetry at increasing transmission energy. This is consistent with the broadening error because skew naturally diffuses over higher distribution spreads. Otherwise, errors in the relative abundance fractions do not demonstrate a strong trend with transmission energy, and all abundance fractions are well-captured. A weak trend also exists with distribution location but with wide error margins; these values are also coupled with the skew parameter, so more analysis is necessary.

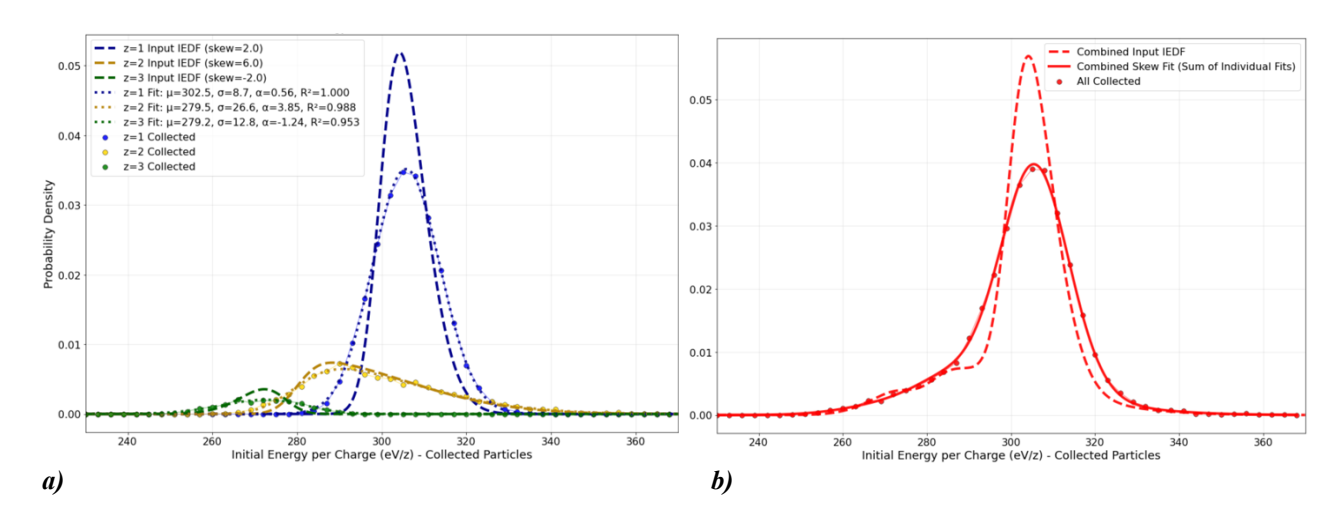


Figure 10. IEPDFs for $\varepsilon_T = 475$ eV/z for (a) species-specific and (b) total (probe construction) distributions.

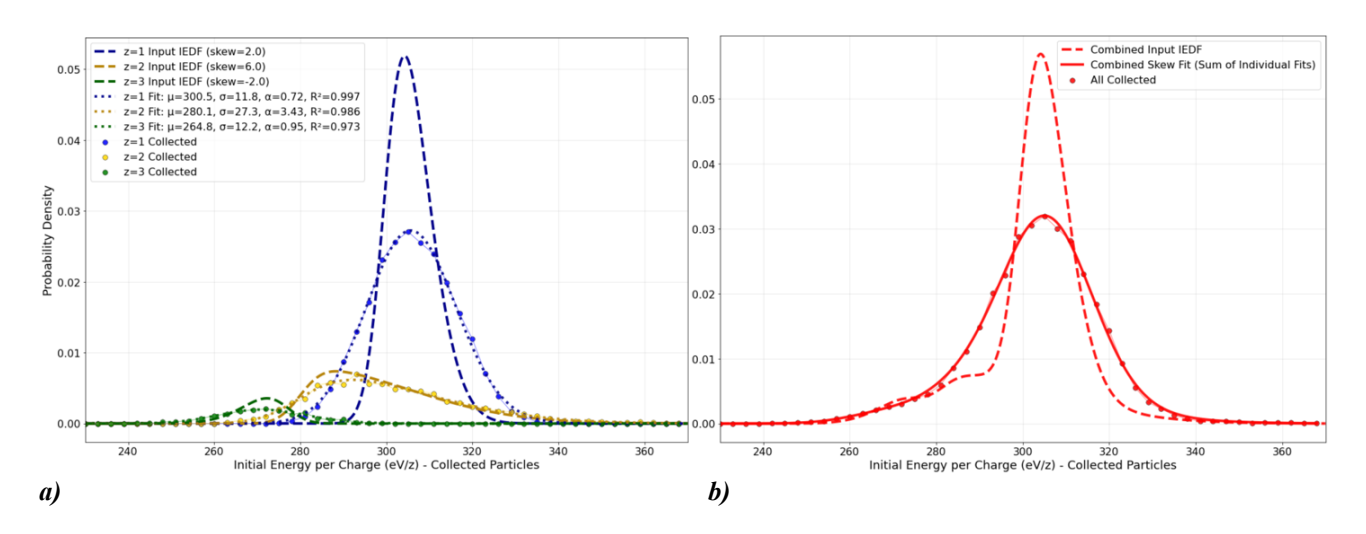


Figure 11. IEPDFs for $\varepsilon_T = 675$ eV/z for (a) species-specific and (b) total (probe construction) distributions.

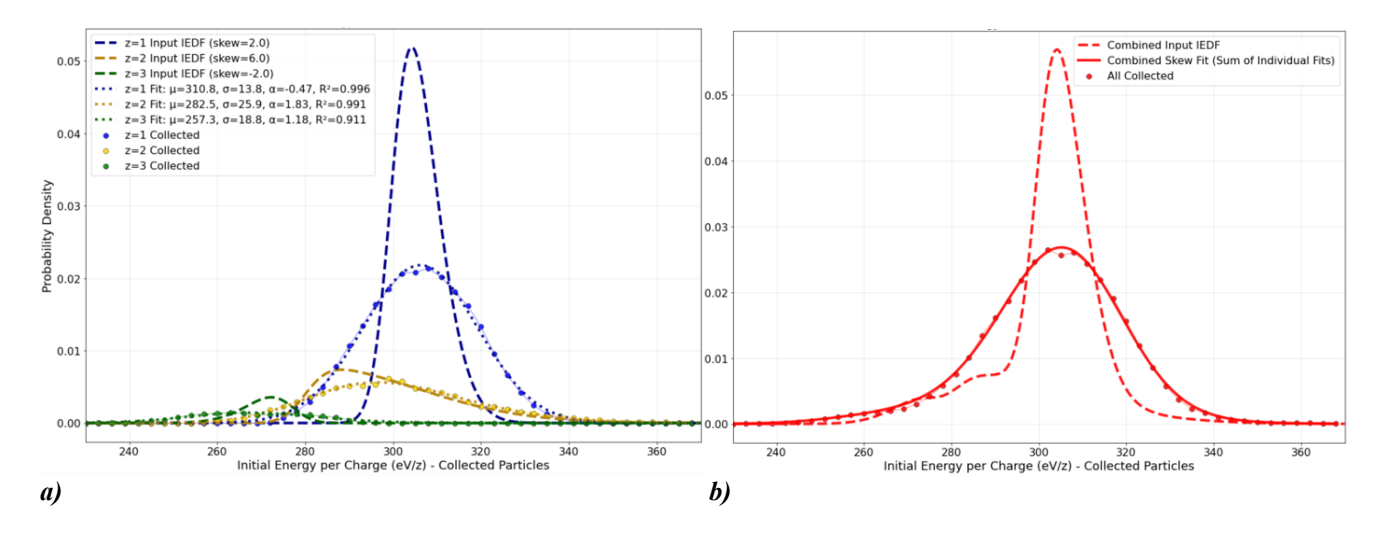


Figure 12. IEPDFs for $\varepsilon_T = 875$ eV/z for (a) species-specific and (b) total (probe construction) distributions.

Table 5. Relative error of output parameters for skew-normal input IEDFs at 475 eV/z, 675 eV/z, 875 eV/z,

	$\varepsilon_T = 475 \text{eV/z}$		
% Error	z=1	z=2	z=3
Location (eV/z)	+ 0.66 ± 0.53 %	-0.25 ± 0.06 %	-0.96 ± 0.27 %
ΔE/E	+ 52.0 ± 3.1 %	+13.94 ± 0.67 %	+55.7 ± 16.0 %
Skew	- 65.7 ± 17.3 %	-27.7 ± 8.2 %	+25.0 ± 24.0 %
Rel. Abund.	-0.036 ± 0.24 %	+ 0.10 ± 0.49 %	0.0 ± 1.7 %

	$\varepsilon_T = 675 \text{ eV/z}$		
% Error	z=1	z=2	z=3
Location (eV/z)	+1.01 ± 0.70 %	+ 0.19 ± 0.20 %	-2.68 ± 3.2 %
ΔΕ/Ε	+ 91.8 ± 2.9 %	-3.03 ± 2.26 %	+ 94.8 ± 20.6 %
Skew	-95.6 ± 3.8 %	-50.1 ± 6.4 %	-112.1 ± 58.4 %
Rel. Abund.	+ 0.26 ± 0.40 %	-0.60 ± 1.14 %	$0.0 \pm 0.0 \%$

	$\varepsilon_T = 875 \mathrm{eV/z}$		
% Error	z=1	z=2	z=3
Location (eV/z)	+2.11 ± 1.4 %	+ 0.86 ± 0.11 %	-4.19 ± 2.0 %
ΔΕ/Ε	+ 134.4 ± 3.1 %	+ 30.3 ± 1.0 %	+149.3 ± 31.3 %
Skew	-100.8 ± 23.2 %	-70.5 ± 2.1 %	+132.1 ± 30.2 %
Rel. Abund.	-0.15 ± 0.18 %	+ 0.012 ± 0.51 %	+ 2.00 ± 1.28 %

B. ExB Reconstruction of IEDFs

Species-specific distributions like those from the ESA sims presented in the Figs. 10a, 11a, and 12a are obscured by the E-VADER experimentalist; the *total* IEDF collection traces shown in Figs. 10b, 11b, and 12b are what is actually generated in a physical ESA experimental run. The simulation allows us to generate the species-specific distributions directly from the ESA scan itself, but in reality, these IEDFs must be reconstructed indirectly from the ExB. It is bias-swept for a select ESA scan voltage, capturing the species breakdown for that slice on the IEDF. 4.5 Performing this over the entire IEDF allows one to construct species-specific distributions. The second inquiry of this research is to determine how well the ExB sector succeeds in this function and to what extent operational input parameters influence its success. For the ExB analysis, the same input distributions are used from the last section, and the transmission energy of 475 eV/z is selected to be analyzed due to its higher fidelity (lower bandpass error) compared to the rest. The complete ExB sweep of the IEDF is performed with 7 eV/z slice intervals and 0.1V-resolution ExB bias steps. Figure 13 presents the ESA-constructed total IEPDF with highlighted energy slices that correspond with charge state distributions (CSDs) simulated by the ExB software presented in Fig. 14.

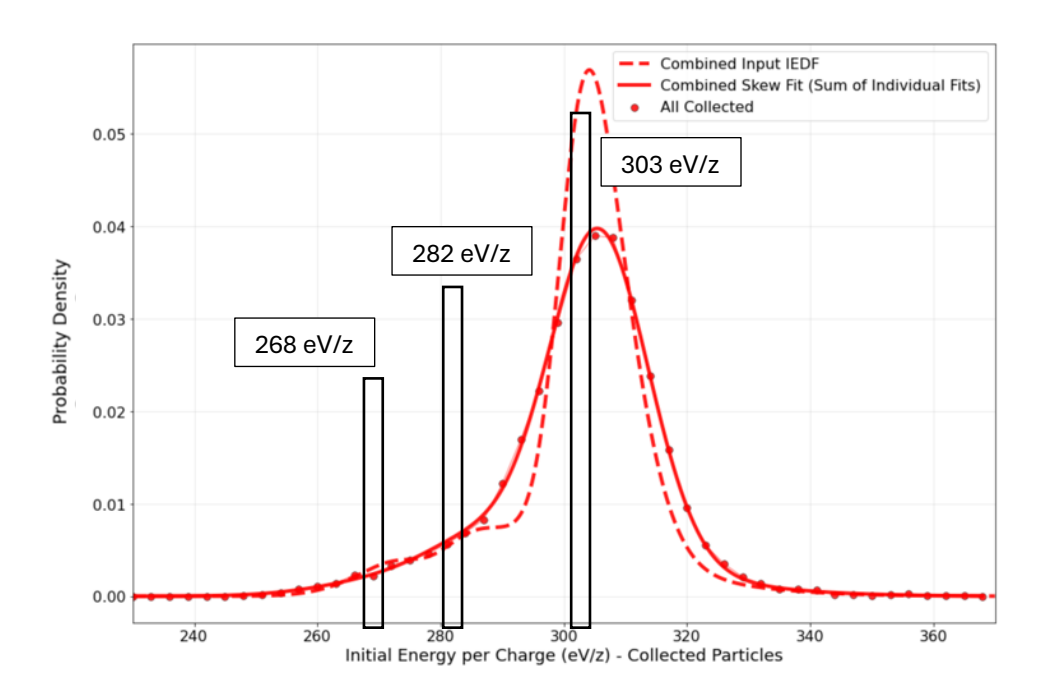


Figure 13. Sample ion energies along ExB sweep on ESA-constructed IEPDF for $\varepsilon_T = 475 \text{ eV/z}$.

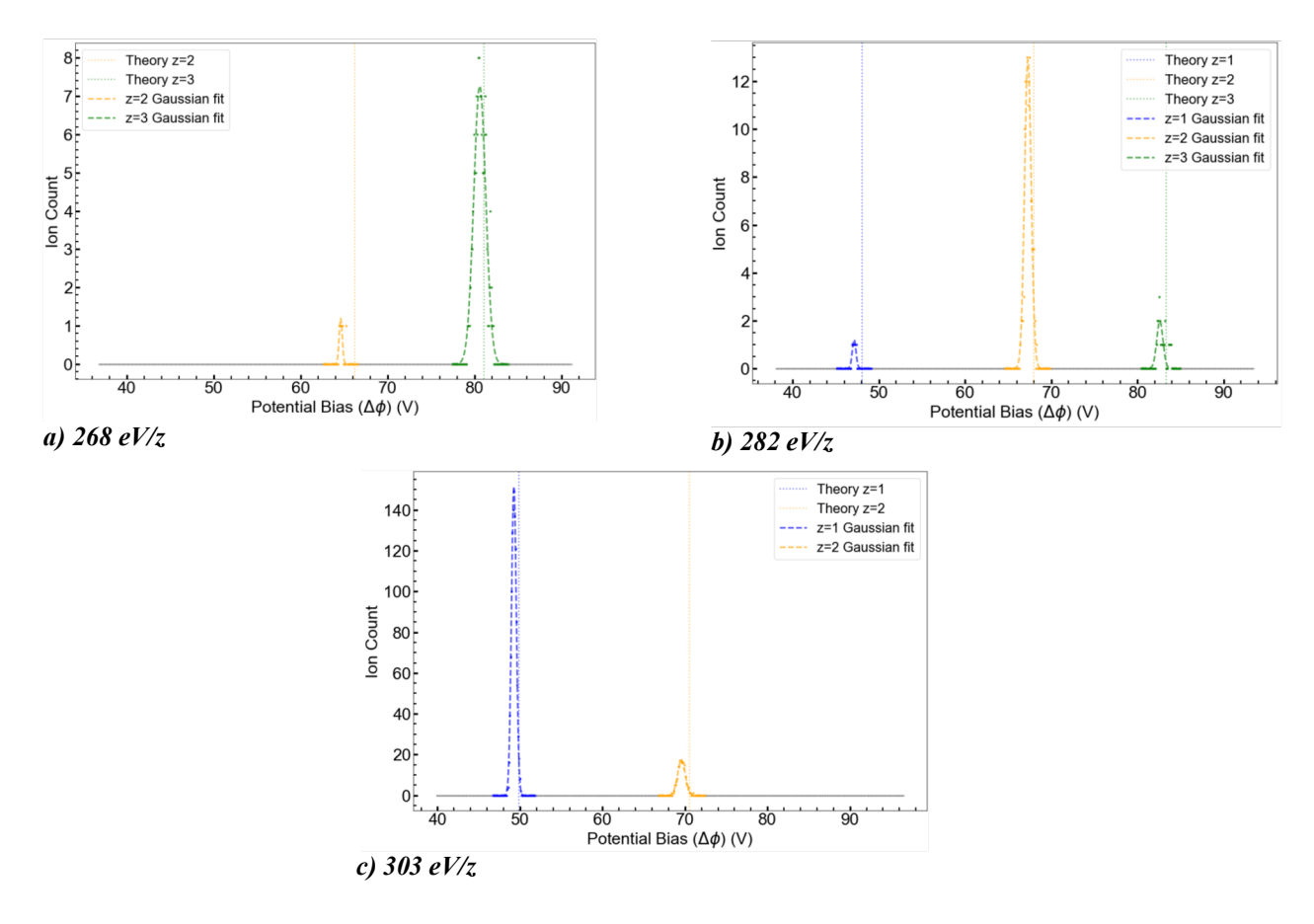


Figure 14. ExB-constructed CSDs for sample ESA slices a) 268 eV/z, b) 282 eV/z, and c) 303 eV/z.

Once the sweep over the entire domain of the IEDF is completed, the sum of ions of each charge state collected at each scan step are area-normalized to its total relative abundance fraction captured by the ExB collector for the entire sweep to convert the collection data to PDFs for like-comparison with the normalized ESA collection result. The outcome of this reconstruction technique is displayed in Fig. 15a, where the ESA-produced species-specific IEPDFs for this operating condition, shown previously in Fig. 6a, is overlayed for comparison. Figure 15b presents a quantitative comparison of the ExB and ESA simulations' constructions of the charge-specific ion energy distributions. It is evident that the ExB reconstruction is over-selecting doubles and triples content relative to the ESA which has accurately collected the ingested z=1, 2, 3 populations with relative input populations 0.70, 0.25, 0.05, respectively. This simulation has been repeated with comparable results.

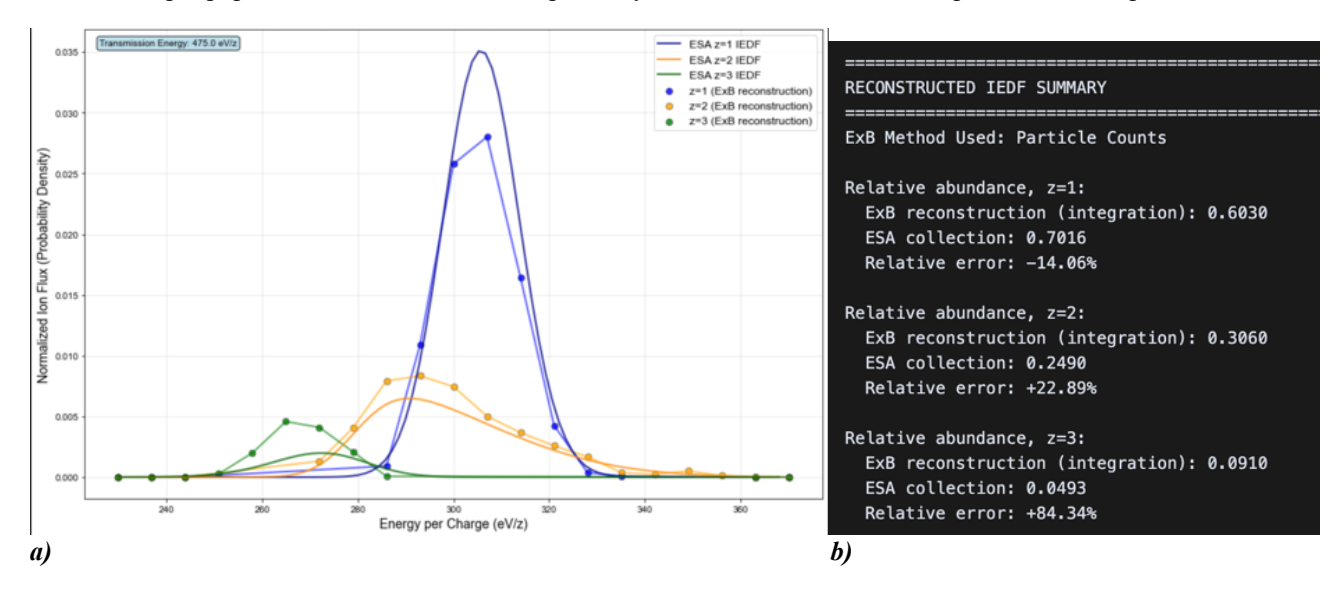


Figure 15. ExB-reconstructed species-specific IEPDFs in comparison with ESA-construction where $\varepsilon_T = 475 \text{ eV/z}$ displayed a) graphically and b) quantitatively

Despite the error present in the previous reconstruction simulation, performing reconstruction on a separate input IEDF parameter set proved more accurate. In Fig. 16, this reconstruction along with its ESA companion is displayed in the same format. It is unclear at this point why this distribution parameter set enable higher accuracy in ExB reconstruction, whether it is a simulation effect or a real result of inequitable treatment of ingested distributions that occurs in the ExB sector. All cases demonstrate high fidelity ESA-constructions of the input species content.

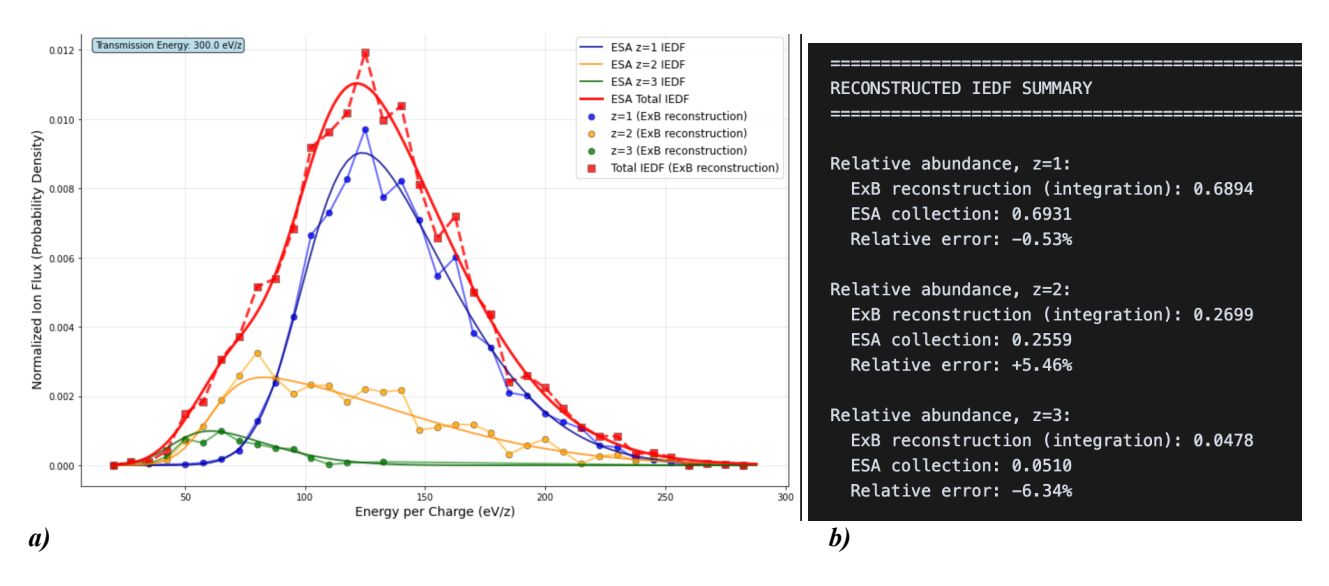


Figure 16. ExB-reconstructed species-specific IEPDFs in comparison with ESA-construction on a disparate input parameter set displayed a) graphically and b) quantitatively.

C. Neutral Density Effects

In the following section a preliminary analysis is presented for how testing a high-power ion engine affects E-VADER charge state measurements. Under these conditions, higher beam current densities will be impinging upon the probe face and entrance collimator. Our emphasis below is placed on what happens inside the probe body. Neutral density accumulation in the probe body is of significant interest due to the inequity of CEX collisional rates across charge species, which will cause charge ratio measurement errors. This is because of the discrepancy in the mean free path lengths of CEX collisions for each charge-species which causes unequal attenuation of species' collection signals as a function of ion travel distance in both probe sectors. The survival equation for ions of charge state z traversing a cloud of neutral particles can be expressed as

$$n_{z_f}(x, E) = n_{z_i} \exp\left(-\frac{x}{\lambda}\right) = n_{z_i} \exp\left(-x \cdot \sigma(E_z) \cdot n_0\right)$$
(10)

where n_z indicates the particle density of charge species z, before and after the ions travel a distance x through a density of n_0 neutral particles with CEX cross section σ , which is dependent on collision energy. It is assumed that any slow neutral that experiences a CEX collision does not have sufficient resulting energy to reach a collector, and the reading is lost. Charge-exchange for z=1 and 2 charge states can be well-approximated in EP plasmas with the reaction equations

$$P^+ + P \to P + P^+$$
 , (11a)

$$P^{++} + P \rightarrow P + P^{++}$$
 , (11b)

for an arbitrary propellant element *P*. In this energy regime, symmetric CEX for doubles proves at least an order of magnitude higher than asymmetric charge transfer, a collision which results in two singles, according to Ref. 8. Neutral density can be assumed isotropic inside the probe body and solved from flux balance into and out of the probe by

$$\frac{1}{4}n_{oin}Av_{th} = \frac{1}{4}n_{oout}Av_{th} + n_i v_i A \qquad , \tag{12}$$

where the LHS is neutral flux-out, and the RHS is flux-in broken into free molecular flow from the facility background gas and the ingestion of ions from the plasma source; ingested ions recombine upon collision with boundaries inside the probe. The background free molecular flow term is dominated by ion ingestion at typical operating facility pressures and current densities at the probe distance, i.e.

$$n_{o_{out}}v_{th} \ll n_i v_i = \frac{j}{e} \qquad , \tag{13}$$

where j is current density at the probe orifice. For example, operating at a high pressure of 100 microtorr and current density of 0.01 A/cm², the ion flux into the probe is two orders of magnitude higher. Equation 12 can then be reasonably simplified to

$$\frac{1}{4}n_{oin}v_{th} = \frac{j}{e} \qquad , \tag{14}$$

and neutral density solved to be

$$n_{o_{in}} = \frac{4j}{v_{th}e} = \frac{4j}{e} \sqrt{\frac{\pi m_0}{8kT_0}} \qquad , \tag{15}$$

with T_0 being the neutral temperature and m_0 the particle mass. Cross section models for single and double CEX given by the reaction expressions 10a,b are obtained for Xenon from Ref. 8, which gives

$$\sigma_{CEX}^{Xe+} = 87.3 + 13.6\log(E)$$
 and (16a)

$$\sigma_{CEX}^{Xe++} = 45.7 + 8.9\log(E)$$
 (16b)

as semi-empirical cross section estimates as functions of bombarding ion energy, E.

Ion-travel distances for the E-VADER from its entrance to the ESA collector and from the ESA collector to the ExB collector are good estimates of the requisite transmission distances, i.e., $x = L_{trans}$ in Eq. (10), required of the ingested ions to avoid charge exchange and induce an output reading on an ammeter. These are given in Table 6 below where charge exchange attenuation values are presented for a set of hypothetical Xe current densities at which the probe is operating; these values represent the ratios of final-to-initial ion species densities from x = 0 to $x = L_{trans}$. Neutral temperature T_0 is estimated to be 300K in all cases. It is evident that at higher-power operating points the discrepancy between the two species' survival becomes pronounced. At 10 mA/cm², the singles are attenuated by a factor of \sim 1.5x more than doubles through the ESA. This would translate to an overprediction of doubles—to—singles on its collector by the same factor, then similar from the ESA to the ExB collector. In summary, at 10 mA/cm² each probe sector induces a roughly equivalent z=2-to-z=1 attenuation ratio of \sim 60% on its passed ions, and for end-to-end – probe entrance orifice to ExB collection – the total attenuation ratio reduces to \sim 37%, meaning singles experience an artificial flux reduction to the ExB collector only 37% the reduction doubles experience.

Table 6: Calculations of attenuation within the E-VADER at varying input beam current density.

Ion Path Distance	ESA	ExB
L_{trans} (m)	0.125	0.147

ESA CEX Attenuation (n_{z_f}/n_{z_i})	$\varepsilon_{trans} = 475 \text{ eV/z}$	
Current Density (mA/cm²)	z=1	z=2
0.01	0.999	1.000
0.1	0.993	0.997
1	0.930	0.973
10	0.485	0.761

ExB CEX Attenuation (n_{z_f}/n_{z_i})	$arepsilon_{trans} = 475 \ \mathrm{eV/z}$	
Current Density (mA/cm²)	z=1	z=2
0.01	0.999	1.000
0.1	0.992	0.997
1	0.918	0.968
10	0.427	0.725

It is evident that the present iteration of this probe will incur serious systematic error at high power due to CEX-induced attenuation. The proposed solution is to "vent" the probe by incorporating another orifice in the probe body out of the line-of-sight of the plume; this would necessitate installation of an electron suppression grid. Consulting the flux balance Eq. 12 presented previously, the additional flux-out term on the LHS associated with this vent aperture would scale down the final expression for the internal neutral density by the factor,

$$\frac{A}{A+A_{vent}} \qquad , \tag{17}$$

meaning that the survival equation, Eq. (10), is in turn scaled closer to unity. Performing the attenuation calculations on a hypothetical design of $A_{vent} = 10A$ – not unreasonable considering the probe's tiny entrance aperture diameter of 15mm – it can be shown that the high-power condition of 10 mA/cm² attenuates the singles' signal by 0.866x and the doubles by 0.898x from entrance to ExB collector. This would result in an overmeasurement of doubles by ~1.04x, a marked improvement over the ~2.70x overmeasurement incurred by the neutral buildup without a venting orifice.

IV. Conclusion and Future Work

This first computational model of the E-VADER—a combined ESA and ExB diagnostic—demonstrates that speciesand charge-state—resolved ion energy distribution functions (IEDFs) can be reconstructed with good accuracy while revealing operating-condition—dependent systematic errors that must be managed in practice. Using Ansys-derived fields with analytical validation and energy-conserving particle pushers (Runge–Kutta for the ESA and Boris for the ExB), we verified correct transmission behavior and recovered input abundance fractions across charge states.

The study shows that increasing transmission energy, ε_T , systematically broadens the reconstructed IEDFs and damps skew; because transmission energy must exceed the highest ion energy per charge to suppress electrons, this broadening is intrinsic; thus, procedure is important. Once more extensive systematic simulations have been carried out across transmission energies, it is the objective of future research to generate uncertainty quantification for the ESA-constructed IEDFs and correct artificial distribution broadening. Moreover, with further study on the influence of various ExB operational parameters (i.e. voltage step size, IEDF reconstruction step size and location), it is desirable to provide concrete best operational practices for accurate species-specific IEDF reconstruction and provide robust UQ, and potentially post-processing error correction, for measurements obtained with select parameter sets.

In the last leg of the presented research, a simple neutral balance coupled with charge-exchange cross sections indicates non-negligible, species-dependent attenuation within the probe body that grows with beam current density and path length. A mitigation approach via probe venting to avoid correction factors derived from measured facility conditions is proposed for future design iteration. A comprehensive incorporation of neutral effects on simulated probe traces is to be developed for upcoming work.

Looking forward, adding collimator transit physics, electron/space-charge effects, and extending inputs to molecular propellants (e.g., H₂O, N₂, air mixtures) will complete the comprehensive modeling of the E-VADER and enable full uncertainty quantification and potential post-correction of physical measurement traces as well as provide design guidance for the next-generation E-VADER.

Acknowledgement

Partial support for this work was provided by NASA contract number 80NSSC21K1118 under the STRI JANUS program lead by Prof. Mitchell Walker at Georgia Tech. This support is gratefully acknowledged.

References

- ¹Farnell, C. C., and Williams, J. D., "Comparison of Hollow Cathode Discharge Plasma Configurations," *31st International Electric Propulsion Conference*, IEPC-2009-016, Ann Arbor, MI, Sept. 2009.
- ²Farnell, C. C., and Williams, J. D., "Comparison of Hollow Cathode Discharge Plasma Configurations," *Plasma Sources Science and Technology*, Vol. 20, No. 2, 2011, Paper 025006. https://doi.org/10.1088/0963-0252/20/2/025006.
- ³Farnell, C. C., Farnell, S. C., and Williams, J. D., "Recommended Practice for Use of Electrostatic Analyzers in Electric Propulsion Testing," *Journal of Propulsion and Power*, Vol. 33, No. 3, 2017, pp. 638–658. https://doi.org/10.2514/1.B35413.
- ⁴Thompson, S. J., Farnell, S. C., Farnell, C. C., and Williams, J. D., "Combined Electrostatic Analyzer—Wien Filter Probe for Characterization of Species Distributions in Hall Thrusters," *Journal of Applied Physics*, Vol. 130, No. 23, 2021, Paper 233302. https://doi.org/10.1063/5.0071656.
- ⁵Thompson, S. J., Farnell, C. C., Williams, J. D., and McHarg, M. G., "Combined Energy and Velocity Analyzer Measurements of a Low-Power Hall Thruster," *37th International Electric Propulsion Conference*, IEPC-2022-404, Massachusetts Institute of Technology, Cambridge, MA, June 19–23, 2022.
- ⁶Shastry, R., Hofer, R., Reid, B., and Gallimore, A., "Method for analyzing ExB probe spectra from hall thruster plumes," 44th AIAA/ASME/SAE/ASEE Joint Propulsion Conference & Exhibit, AIAA-2008-4647, Pasadena, CA, Jul. 2008.
 - ⁷Brieda, L., *Plasma simulations by example*, Boca Raton: CRC Press, 2021.
- ⁸Miller, J. S., Pullins, S. H., Levandier, D. J., Chiu, Y., and Dressler, R. A., "Xenon charge exchange cross sections for electrostatic thruster models," *Journal of Applied Physics*, Vol. 91, Feb. 2002, pp. 984–991.